Effect of thermal aging on microstructure and carbides of SA508/Alloy 52 dissimilar metal weld

Materials Characterization 200 (2023) 112880

Contents lists available at ScienceDirect

Materials Characterization

journal homepage: www.elsevier.com/locate/matchar

Effect of thermal aging on microstructure and carbides of SA508/Alloy 52 dissimilar metal weld

Y. Ge [a], Z. Que [a,*], K. Lindgren [b], N. Hytönen [a], M. Thuvander [b]

[a] Advanced Materials for Nuclear Energy, VTT Technical Research Centre of Finland, Kivimiehentie 3, FI-02044 VTT, Finland
[b] Microstructure Physics, Department of Physics, Chalmers University of Technology, Göteborg 412 96, Sweden

ARTICLE INFO

Keywords:
Dissimilar metal welds
Thermal aging
Alloy 52
Carbides
Narrow gap

ABSTRACT

A narrow-gap SA508/Alloy 52 dissimilar metal weld (DMW) mock-up, fully representative of an actual nuclear component, was investigated in this work. The microstructure and carbides formed in the low alloy steel fusion boundary (FB) and heat affected zone (HAZ) can act as brittle fracture initiators and could influence the brittle fracture behavior. However, the amount of information available in the open literature on the microstructural changes and carbide formation in DMW occurring upon post-weld heat treatment and long-term thermal aging is very limited. The microstructure and carbide type, morphology and size in the carbide precipitation zone (CPZ, up to 1.5 μm from FB), carbon depletion zone (CDZ, up to 40–50 μm from FB) and HAZ (up to 2 mm from FB) of the plant-relevant DMW in post-weld heat-treated and thermally-aged (400 °C for 15,000 h, corresponding to 90 years of operation) conditions were analyzed with analytical electron microscopy, wide-angle X-ray scattering and atom probe tomography. Long-term thermal aging increases the microhardness peak close to the FB, triples the width of the CPZ and coarsens the carbide size in the HAZ (up to a magnitude). There is no evidence of a significant phosphorus segregation to grain boundaries due to thermal aging.

1. Introduction

Dissimilar metal welds (DMWs) are commonly used to join austenitic and ferritic/bainitic components in the nuclear reactor coolant pressure boundary with a Ni-based filler metal [1] [2] [3]. The crystallographic difference and the chemical composition gradient (specifically C and Cr) at the fusion interface between the bainitic reactor pressure vessel steel and the austenitic weld metal results in a complex fusion boundary (FB) microstructure and a mismatch of corrosion and strength at the interfaces [4] [5] [6] [7]. DMWs are critically influencing the structural integrity of the nuclear power systems, structures and components [8] [9] [10].

The carbides formed at the FB and in the low alloy steel (LAS) heat affected zone (HAZ) can act as brittle fracture initiators and thus the type, morphology and size of carbides significantly influence the brittle fracture behavior [11]. In addition, hardness mismatch at the DMW FB was governed by the change of precipitate morphology and size due to dislocation cutting or bowing phenomena [12]. However, the amount of information available in the open literature on the microstructural changes and carbide formation occurring at the FB upon post-weld heat treatment (PWHT) and during long-term thermal aging is very limited [3] [13] [14] [15]. Furthermore, the segregation of impurity elements (*e.g.* phosphorus) during heat treatment and aging and carbon diffusion from LAS to Alloy 52, are known to increase susceptibility to cracking and stress corrosion cracking [16] [17]. Moreover, the narrow-gap (NG) weld without buttering and subsequent PWHT exhibits different microstructures at the FB and HAZ compared to Alloy 52 buttering welding technique [18] [19]. Understanding the effects of long-term thermal aging on the detailed FB microstructures and carbide formation are crucial for the integrity evaluation and safe long-term operation of nuclear components with NG DMW [20] [21].

Lindqvist et al. [22] [23] reported that for NG SA508/Alloy 52 DMW, when the notch of the fracture toughness T_0 test is placed in the HAZ near the FB, the brittle fracture crack deviates to the FB after initiation and propagates along the FB in most cases. However, if the notch has a distance to the FB $\gtrsim 0.3$ mm, the crack does not deviate to the FB and has a crack path parallel to the FB, which ends up with very low fracture toughness. This work reveals that the investigation of brittle fracture behavior and the knowledge of microstructure and carbide formation in both near FB region and HAZ are important in respective of structural integrity.

In this work, the microstructure and carbides' crystal structure,

* Corresponding author.
E-mail address: zaiqing.que@vtt.fi (Z. Que).

https://doi.org/10.1016/j.matchar.2023.112880
Received 13 January 2023; Received in revised form 18 March 2023; Accepted 31 March 2023
Available online 5 April 2023

chemistry, morphology and size in the LAS FB carbide precipitation zone (CPZ, normally up to 1.5 μm from FB), carbon depletion zone (CDZ, up to 40–50 μm from FB) and HAZ (up to 2 mm from FB) were analyzed. Advanced characterization including analytical electron microscopy, wide-angle X-ray scattering (WAXS) and atom probe tomography (APT) were applied. The effects of long-term thermal aging on the microstructures and carbide formation and the fracture mechanical behavior are discussed.

2. Experimental methods and materials

2.1. Materials

In this study, a 1:1 scale DMW safe-end mock-up fully representative of an actual component in a Finnish nuclear power plant is investigated [24] [25]. The figure of the structure of the DMW mock-up investigated in this study is presented in Fig. 1. The technical details of the DMW mock-up are given in Table 1. The chemical compositions of the materials are given in Table 2.

The mock-up is a NG DMW full-scale pipe mock-up provided by TVO. It consists of an Alloy 52 (UNS N06052) NG weld joining SA508 nozzle and stainless steel AISI 316LN safe-end. The inner surface of the LAS wall has a 308L stainless steel cladding. The mock-up is welded one bead per layer and is ~9 mm wide and ~ 94 mm thick. The welding was performed in circumferential direction and the weld was post weld heat-treated at 550 °C for 15 h and 610 °C for 7 h. The investigated conditions are as-received post weld heat-treated condition ("NG AR") and the thermally aged condition after 15,000 h at 400 °C ("NG TA"). This thermal aging corresponds to 90 years of nuclear power plant operation, when the P segregation at grain boundaries is considered as the main aging mechanism [19].

2.2. Microstructural characterization

The Vickers micro-hardness measurements with loads of 1 kg (HV1) and 0.3 kg (HV0.3) across the FB were performed using a Struers DuraScan-80 device.

Table 1
Technical details of the NG mock-up investigated.

	NG mock-up
Nozzle	SA508 gr.2
Cladding	SS308L/309 L
Weld	Alloy 52 narrow-gap
Safe-end	AISI 316LN
PWHT	17 h at 550 °C + 7 h at 610 °C
Welding method	TIG welding
Conditions	PWHT or thermally aged at 400 °C for 15,000 h

The specimens were cut by electrical discharge machining to a thickness of ~0.5 mm and mechanically thinned from both sides to ~100 μm. The final thinning was carried out by twin jet electropolishing using a Struers TenuPol-5 electropolisher with an electrolyte consisting of 1 M concentration of NaCl in ethylene glycol and 200–400 mL ethanol. Some thin foils were further ion milled to obtain a thin area near the FB by Gatan Precision Ion Polishing System (PIPS, model 691).

Transmission electron microscopy (TEM) was used to characterize the carbides. Scanning TEM (STEM) high-angle annular dark-field (HAADF) and bright-field (BF) images and chemical information of carbides were acquired on FEI Talos F200X STEM equipped with Super-X EDS system operating at 200 kV. A Zeiss Crossbeam 540 scanning electron microscope (SEM) equipped with an energy dispersive X-ray spectroscopy (EDS) system was used for baseline microstructural characterization for all TEM foils.

WAXS was performed with a Xenoxs Xéuss 3.0 system with Mo tube. Selected TEM foils were also studied with WAXS in transmission mode with a Mo tube of 700 μm beam size. The measured area is located at the HAZ. The 2D WAXS patterns are integrated and converted into 1D profiles and refined with MAUD program [26].

The APT specimens were electropolished using a standard two-step method. A LEAP 3000X HR with a detection efficiency of 37% was used for the APT analysis. The pulse frequency was 200 kHz, the pulse fraction was 20%, and the temperature 70 K. For the reconstruction and analysis, IVAS 3.6 was used. Care was taken for the analysis of the P content. P evaporated mostly as P^{2+} and P^{3+}. P^{+} was also included in the

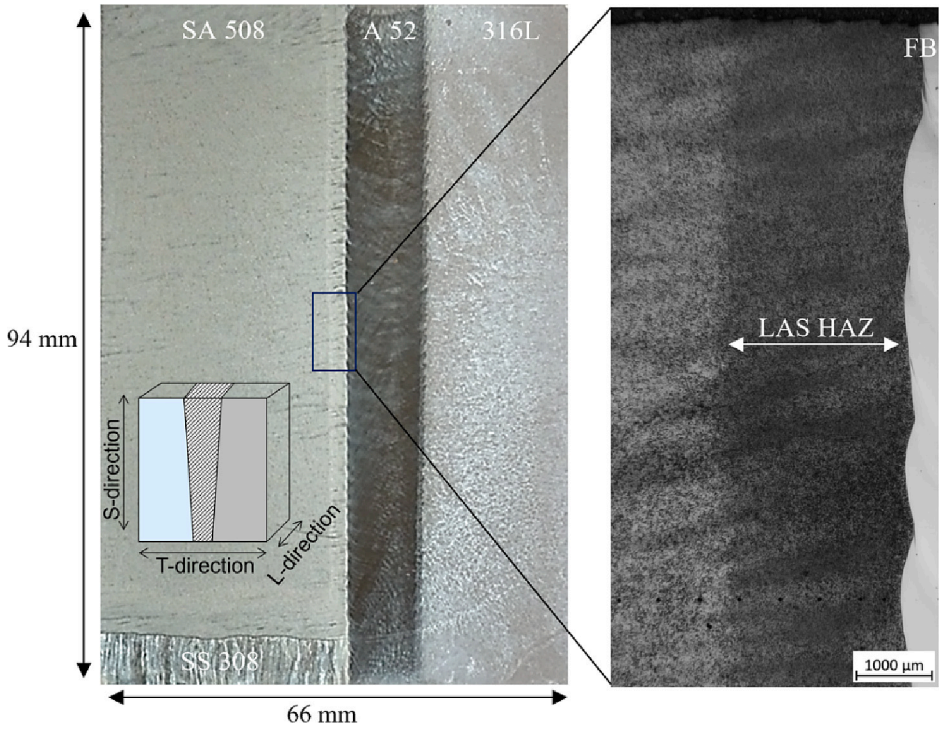

Fig. 1. NG welded dissimilar joint of the investigated mock-up.

Table 2
Chemical composition of the mock-up LAS nozzle material and Alloy 52 weld in weight%.

	C	Cr	Mo	Ni	Mn	Si	P	S	Al	Ti	Cu	V	Fe
SA508	0.18	0.12	0.49	0.78	1.49	0.19	0.005	0.001	0.02	0.002	0.06	–	Bal.
Alloy 52	0.023	29.93	<0.01	Bal.	0.26	0.15	<0.005	0.0007	0.66	0.54	<0.01	–	10.4

deconvolution of peaks as it overlaps with Ni^{2+}. It was found to not give a significant contribution to the P content.

3. Results

3.1. DMW general microstructure and microhardness

The microhardness profiles of HV1 and HV0.3 across the FB in the NG AR and NG TA samples are shown in Fig. 2. The microhardness peaks are close to the FB of the LAS side in both materials. The HV1 and HV0.3 profiles are rather similar. It is evident that the NG TA material has a higher microhardness peak (~20 HV) than the NG AR material and the position of the peak hardness is closer to the FB in the NG TA material.

As shown in Fig. 3, the general microstructure and precipitations of the FB CPZ (0.5–1.5 μm from FB), CDZ (40–50 μm from FB) and HAZ (up to 2 mm from FB) of SA508/Alloy 52 were investigated using TEM foils with SEM. At the FB of the LAS side, a fine CPZ about a few hundred nanometer wide was formed (more discussion in Chapter 3.2). It is noted the fine carbides in the CDZ (more discussion in Chapter 3.3) are mostly located in small grains whereas large grains are almost carbide free. In the HAZ (more discussion in Chapter 3.4), the grain size is further decreased with increased distance to the FB and the carbide distribution tends to be more homogeneous. Carbides are formed both at grain boundaries and within grains in the HAZ. A moderate difference in the microstructure in the CDZ and HAZ was observed in the AR and TA materials. The width of CDZ is slightly narrower for the TA material than the AR material and the grain size shows a larger variation in the CDZ of the AR material. The reduction of the width of the CDZ implies a continuous diffusion of C from the CDZ to the CPZ during long-term thermal aging.

3.2. CPZ microstructure and carbide analysis

The microstructure and carbide formation at the FB CPZ (0.5–1.5 μm from the FB) were investigated with SEM and TEM. An intensive carbide accumulation area (CPZ) is found in both AR and TA materials due to the high content of the strong carbide-forming element Cr at the FB as shown in Fig. 4. Though the width of the CPZ varies locally along the FB, there is a clear difference in the CPZ width between AR and TA materials. As shown in Fig. 4, the CPZ of the AR and TA materials is up to 500 nm and >1500 nm, respectively. The number of carbides is much lower and the size of the carbides is also smaller in the AR material compared to the TA material. The elemental maps in Fig. 4 reveal that the carbides are (Fe, Cr, Mn) carbides with higher Cr than Mn content. In addition, the NG TA material contains Mo-rich carbides and Cr-rich carbides, which are also found at grain boundaries of Alloy 52.

TEM BF images and elemental maps in Fig. 5 reveal the carbides at the FB between LAS and Alloy 52 in the NG AR material. The FB is determined in the image by selected area electron diffraction (SAED) patterns, which show LAS with body centered cubic (BCC) lattice at the left side and Alloy 52 with face center cubic (FCC) lattice at the right side. Near the FB, the BCC grains are columnar with a similar orientation. Nanometer-sized Cr nitrides (≤ 30 nm) with both rod shape and round shape were found in the columnar grains next to the FB at the LAS side. The Mo content in these nitrides is also slightly higher than in the matrix. Enriched Ni and Mn islands are found inside the BCC phase at the FB. Moreover, the Ni and Mn elements were found to segregate at the FBs and boundaries of islands as illustrated in the line profile of Fig. 5 (d). Except these island areas, the Ni and Cr contents continuously decrease with increasing distance from the FB. In this imaged area only one (Fe, Cr, Mn) carbide of about 40 nm size is found at the lower left corner with higher Cr content than the Mn content. It is noted that a quite high dislocation density is observed in both the FCC and BCC phases near the FB. The SAED pattern in Fig. 5(c) is from one (Fe, Cr, Mn) carbide, where weak reflections can be indexed with M_3C type carbide along zone axis [$11\bar{1}$] and strong reflections from surrounding BCC grains that are close to the ⟨111⟩ zone axis.

The FB CPZ microstructure revealed by TEM is in good agreement with the SEM observations in Fig. 4. The nanometer-sized Cr nitride accumulated area extends about 100 nm and locally up to 300 nm from the FB. Carbides, rich in Fe, Cr and Mn, dominate in the region about 200–500 nm from the FB together with additional nanometer-sized nitrides and carbides. Therefore, the CPZ is about 400–500 nm wide between the FB and the CDZ in the NG AR material.

The Cr content in the $(Fe, Cr, Mn)_3C$ carbides continues to decrease as the Cr concentration decreases in the matrix with increasing distance

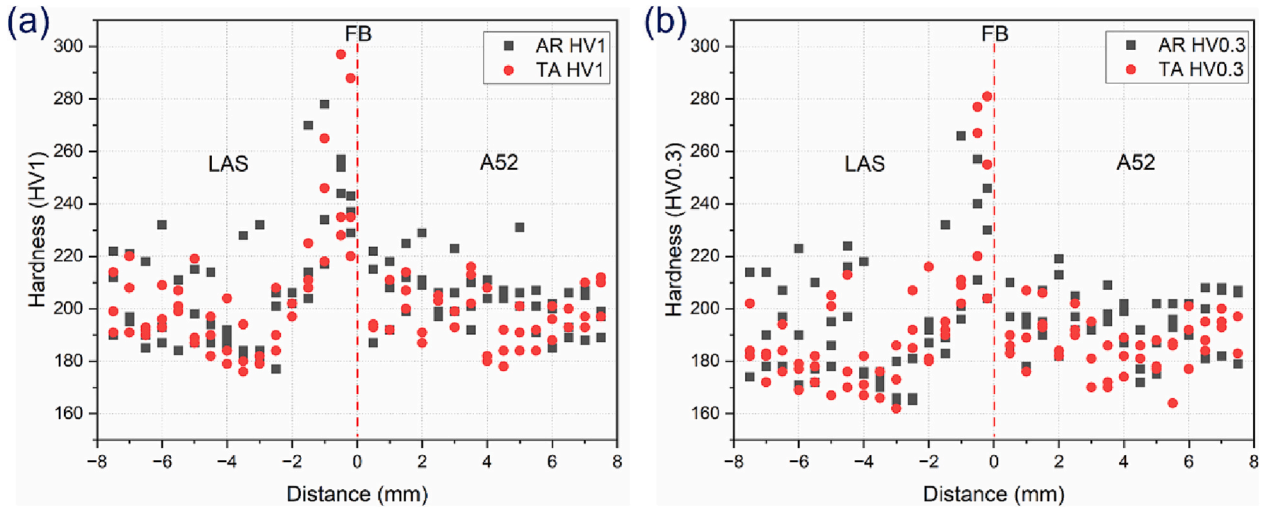

Fig. 2. Microhardness profiles of HV1 and HV0.3 across the FB in the NG AR and NG TA samples.

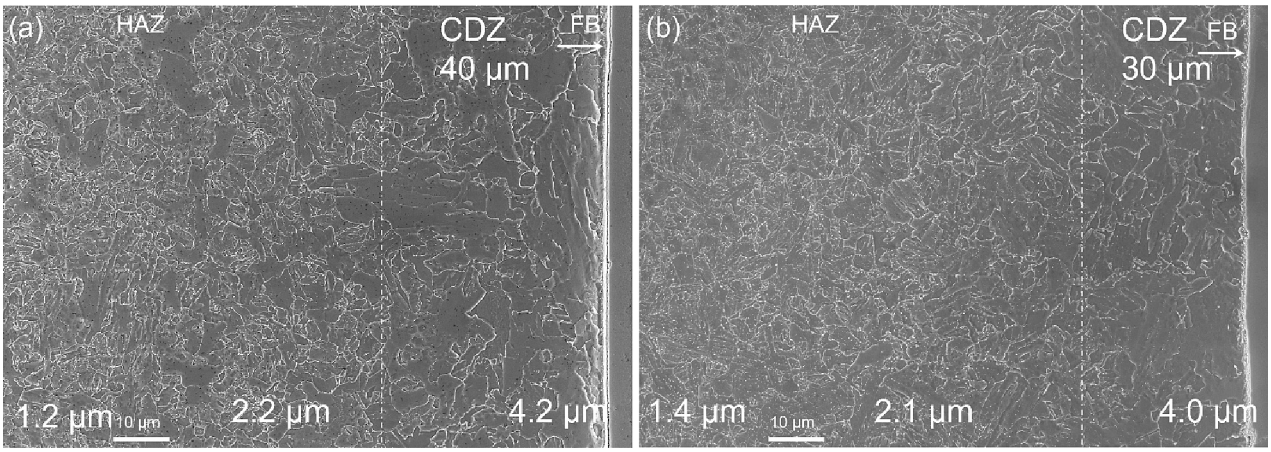

Fig. 3. SEM images (using secondary electrons (SEs)) show the grain size distribution and CDZ width in the LAS. (a) NG AR and (b) NG TA.

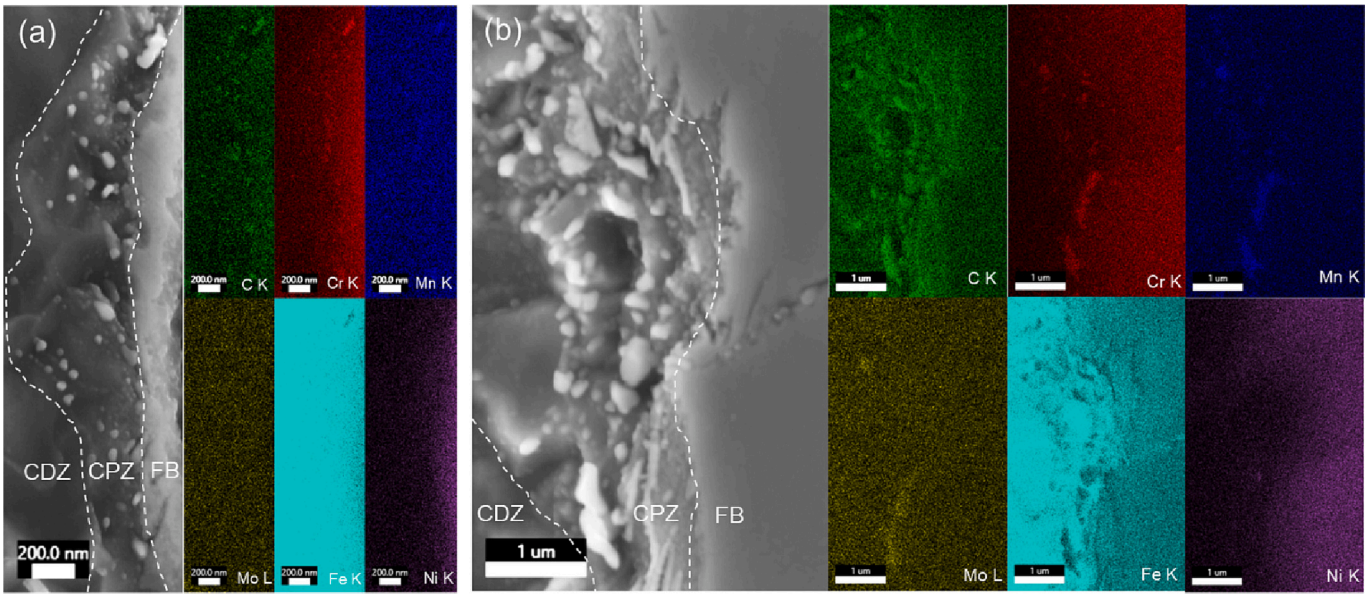

Fig. 4. SEM/EDS elemental maps of carbides at the FB of the LAS. (a) NG AR and (b) NG TA.

from the FB. The microstructure and the carbides at the interface of the CPZ and CDZ are shown in Fig. 6(b). Except a few nano-sized nitrides, carbides are almost invisible in the neighbor CDZ grains. The majority of these carbides are relatively large with a size range of 50–100 nm. A SAED pattern with a large selected-area aperture confirms that these carbides are M_3C type of θ phase (*i.e.*, cementite). The Cr concentration is higher than the Mn in almost all carbides next to the FB as seen in Fig. 5, whereas the carbides next to the CDZ have a slightly higher Mn content than Cr, see Fig. 6. The Cr/Mn ratio of the carbides at the interface between the CPZ and CDZ is normally very close to the Cr/Mn ratio in the surrounding matrix. However, it has been observed that when the Cr/Mn ratio is lower than 1.5 in the matrix, carbides with Cr/Mn ratio below 1 can be formed. This can be seen from the extracted line profile that crosses through a Cr nitride, a high Cr/Mn ratio (>1) carbide and a low Cr/Mn ratio (<1) carbide. Tiny nano-particles about a few nm containing mainly Ti are also visible in this area. The number of Mo-rich carbides along the interface between the CPZ and CDZ is notably higher than at the FB.

Nano-particles are also found at the FB in the NG TA material, as shown in Fig. 7. In contrast to the NG AR material, these nano-particles are carbides instead of nitrides. As shown in the N elemental map in Fig. 7(b), only noisy background counts were detected. Moreover, these carbides belong to Cr-rich and Mn-rich carbides, respectively. The combined maps and line profiles reveal that the compositions are different in these two kinds of carbides. The Mn-rich carbides contain a small Ni content whereas the Cr-rich carbides contain a small amount of Mo. Ni and Mn are clearly segregated at the FB. The SAED pattern along [113] zone axis of the BCC phase shows two additional spots located at 1/3 and 2/3 of the BCC reflection $1\bar{1}21$. The DF image from 1/3 $1\bar{1}21$ confirms that the two extra spots are from nano-carbides. It can be indexed as M_3C θ carbides according to Bargaryatskii's orientation relationship [27] between θ and α, *i.e.* $[001]_\theta \,||\, [011]_\alpha$ and $(010)_\theta \,||\, (21\bar{1})_\alpha$. According to this orientation relationship, for BCC [113] zone axis, the M_3C is close to [102] zone axis with a 3.4° deviation, resulting in only one systematic row along the 010* direction under this diffraction condition. In other words, in this particular orientation, $[102]_\theta$ is about 3.4° away from $[113]_\alpha$ and $(060)_\theta \,||\, (1\bar{1}21)_\alpha$. Similar to the NG AR material, Ti-rich nano-particles with about a few nm size are visible in both BCC and FCC phases. The density of nanometer-sized carbides decreases gradually with increasing distance from the FB. The area containing accumulated nanometer-sized carbides extends >1 μm from the FB in the NG TA material, which is much wider than in the NG AR material.

The CPZ normally extends to around 1.5 μm from the FB in the NG

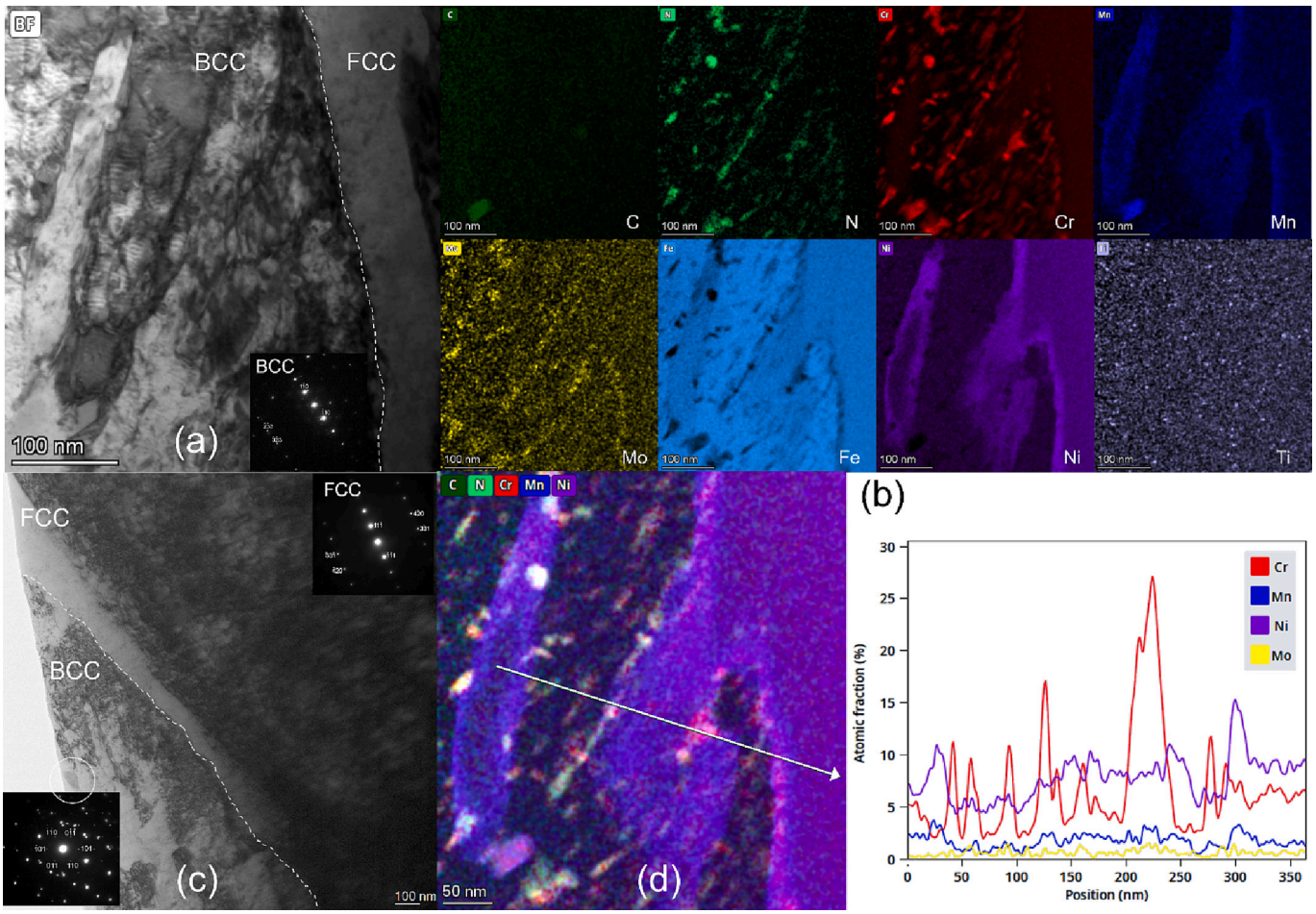

Fig. 5. Carbides at the FB in the NG AR material. (a) STEM BF image and (b) the corresponding elemental maps; (c) TEM BF image and SAED pattern of one large carbide of M_3C type along zone axis [11¯1]; (d) Combined carbides and nitrides maps and extracted line profile reveal elemental variation across the FB and nano-sized particles.

TA material. However, when the tempered martensite type of FB was formed instead of a narrow fusion line (as in most cases), the CPZ can be as wide as about 11 μm, as revealed by Fig. 8. At the interface of the CPZ and CDZ (next to the tempered martensite type of the FB), the number of carbides significantly decreased and almost disappear in the neighbor CDZ grains, as shown in Fig. 9. Tempered martensite laths with high dislocation density are aligned approximately parallel to the interface in Fig. 9. The tempered martensite laths are full of carbides with higher Cr content than Mn. The dominated carbides in the CPZ are $(Fe, Cr, Mn)_3C$ carbides of M_3C type. However, at the interface of the CPZ and CDZ, the Mn content in the carbides becomes higher than the Cr content and the Cr/Mn ratio in matrix is about 1.5. Nitrides are not found at the interface of the CPZ and CDZ. However, the N map illustrates that the nanometer-sized nitrides formed together with carbides at lath boundaries in the CPZ. Ni-rich particles are also observed in carbides especially at lath boundaries. It is noted that Mo carbides start to form at the interface between the CPZ and CDZ.

3.3. CDZ microstructure and carbide analysis

Fig. 3 and Fig. 4 show that no apparent carbides are visible in the CDZ in SEM images. Due to the limited resolution of SEM, it only indicates that no carbides with size larger than 100 nm are present. TEM examination of the CDZ area reveals that there are carbides in the CDZ but with much lower density and smaller size compared with carbides near the FB. In contrast to the difference in width of the CDZ, the carbide distribution in the CDZ in the NG AR and NG TA materials is quite similar, as shown in Fig. 10 and Fig. 11, respectively. In Fig. 10(b) and Fig. 11(b), the observed carbides are mostly Mo carbides with few (Fe, Mn, Cr) carbides located at grain boundaries. It is worth noting that $(Fe, Cr, Mn)_3C$ carbides dominate in the CPZ where the Cr content is higher than that of Mn. However, for the $(Fe, Mn, Cr)_3C$ carbides in the CDZ, the Mn content is much higher than that of Cr. The line profile of the carbides shows that the Cr content in the carbides is just slightly higher than in the matrix. The size of $(Fe, Mn, Cr)_3C$ carbides in the CDZ are normally $\leq$50 nm and the size of the Mo carbides is mostly only a few nanometers.

3.4. HAZ microstructure and carbide analysis

From the CDZ to the HAZ (outside the CDZ), the carbide population increases dramatically. The microstructure and carbide distribution in the HAZ of the NG AR and the NG TA materials are illustrated in Fig. 12. SEM images show two kinds of grains, *i.e.* grains with excess carbides and grains lacking apparent carbides. High-resolution TEM reveals that these grains lacking apparent carbides may contain nano-sized carbides. It is worth to note that the fraction of grains devoid of visible carbides in the HAZ is 2–3 times higher in the NG TA material than in the NG AR material. The STEM image of Fig. 12(d) shows a few long fiber-like carbides aligning in same direction, with the longest one up to 2 μm in length, which is a magnitude longer than in Fig. 12(b). It seems that these long carbides were formed during thermal aging.

The TEM-EDS elemental maps in Fig. 13 illustrate the morphology and distribution of carbides in the HAZ of the NG AR material, where

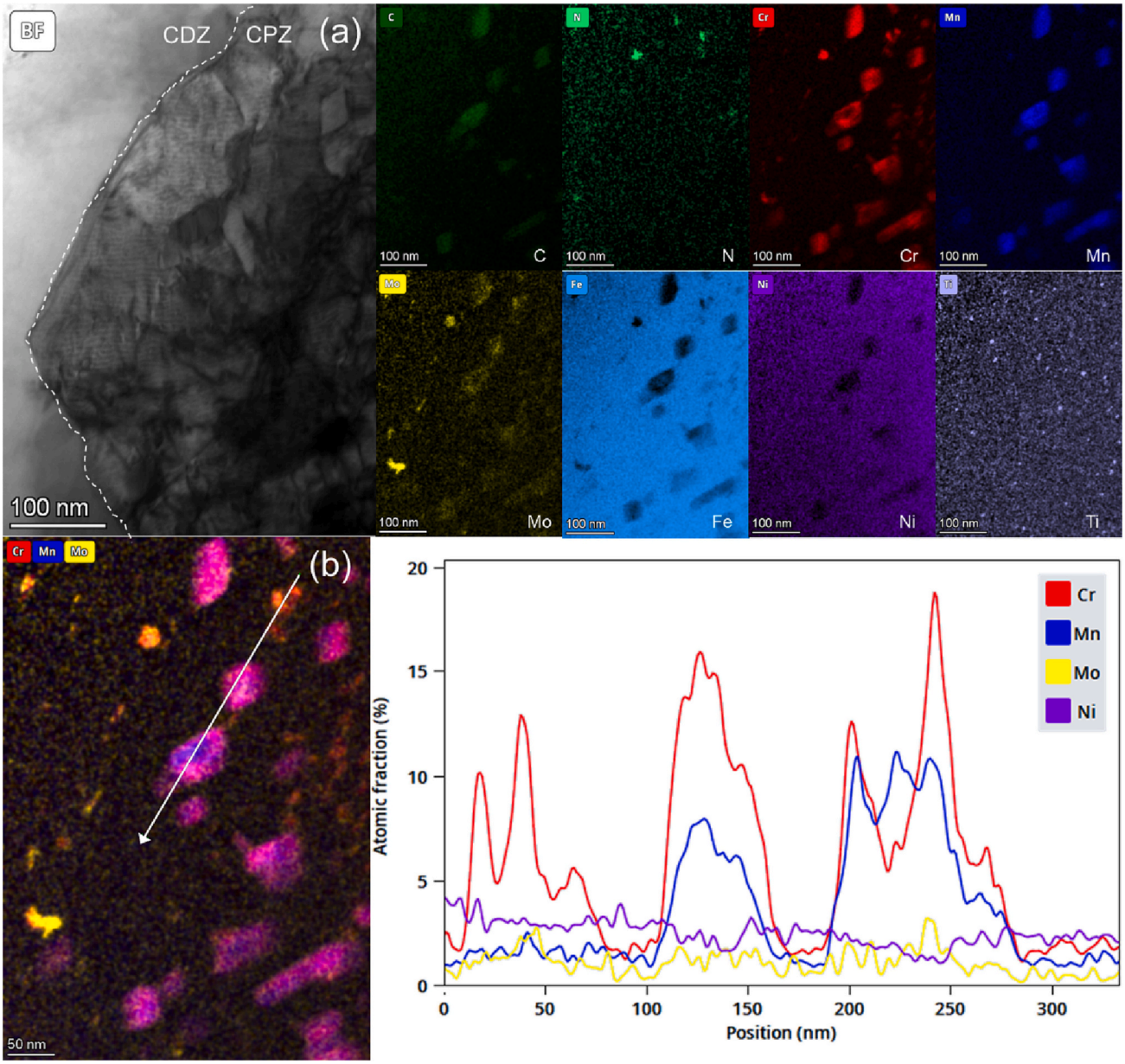

Fig. 6. Carbides at the interface of CPZ and CDZ in the NG AR material. (a) STEM BF image and corresponding elemental EDS map; (b) Combined Cr, Mn and Mo maps and extracted elemental profile from the line marked in the color map.

excess carbides can be found both at grain boundaries and within grains. There are two size groups of carbides, *i.e.*, relatively small carbides and relatively large carbides in the HAZ. The dominant and large-size carbides range from tens to hundreds of nanometers. They have a round or ellipsoidal shape and are found both at grain boundaries and within grains. The elemental maps and the extracted line profile in Fig. 13 reveal that the large carbides are (Fe, Mn, Cr)$_3$C carbides with the content of Mn being much higher than the Cr content. Only occasionally, carbides with Cr content higher than Mn are observed (few carbides containing high-Cr core particles). The relatively small carbides are Mo-rich carbides. The majority of the Mo carbides are located at grain boundaries and their size is about a few tens of nm. Fig. 13 reveals additionally Al—Si nano-sized particles with a few nm to a few tens of nm in size. The SAED in Fig. 13(b) consists of two phases, the major reflections from BCC along [102] zone axis and the weak spots from Mo_2C along [100] zone axis. A few Mo_2C particles are illustrated in the DF image with Mo_2C $00\bar{2}$ reflection.

To investigate the crystal structure of the (Fe, Mn, Cr)$_3$C carbides in the NG AR material, one large and isolated particle was tilted along the zone axis [$11\bar{0}$], which confirmed the M_3C crystal structure in Fig. 14. The DF image from the reflection of $1\bar{1}\bar{1}$ reveals a low angle boundary in the particle. The lattice parameters deviated slightly from the lattice of stoichiometric Fe_3C.

The chemical composition of the long fiber-like carbides with a length up to 2 μm in the HAZ of the NG TA material is presented in the TEM EDS mapping in Fig. 15. They are (Fe, Mn, Cr)$_3$C carbides with a Cr content slightly higher than the matrix. The extracted line profile shows that the width of these carbides is between 50 and 100 nm. Most of the Mo carbides are a few tens of nm in size but a few of them are needle-like and extend over 100 nm. Such needle-like Mo carbides are not observed in the NG AR material.

SAED patterns from two separated carbides in the HAZ of the NG TA sample examined with different zone axes are presented in Fig. 16(a,b). Both zone axis patterns can be indexed with M_3C lattice and the lattice parameters agrees perfectly with stoichiometric Fe_3C. Fig. 16(c) illustrates a high-resolution fringe image of one Mo carbide and its fast

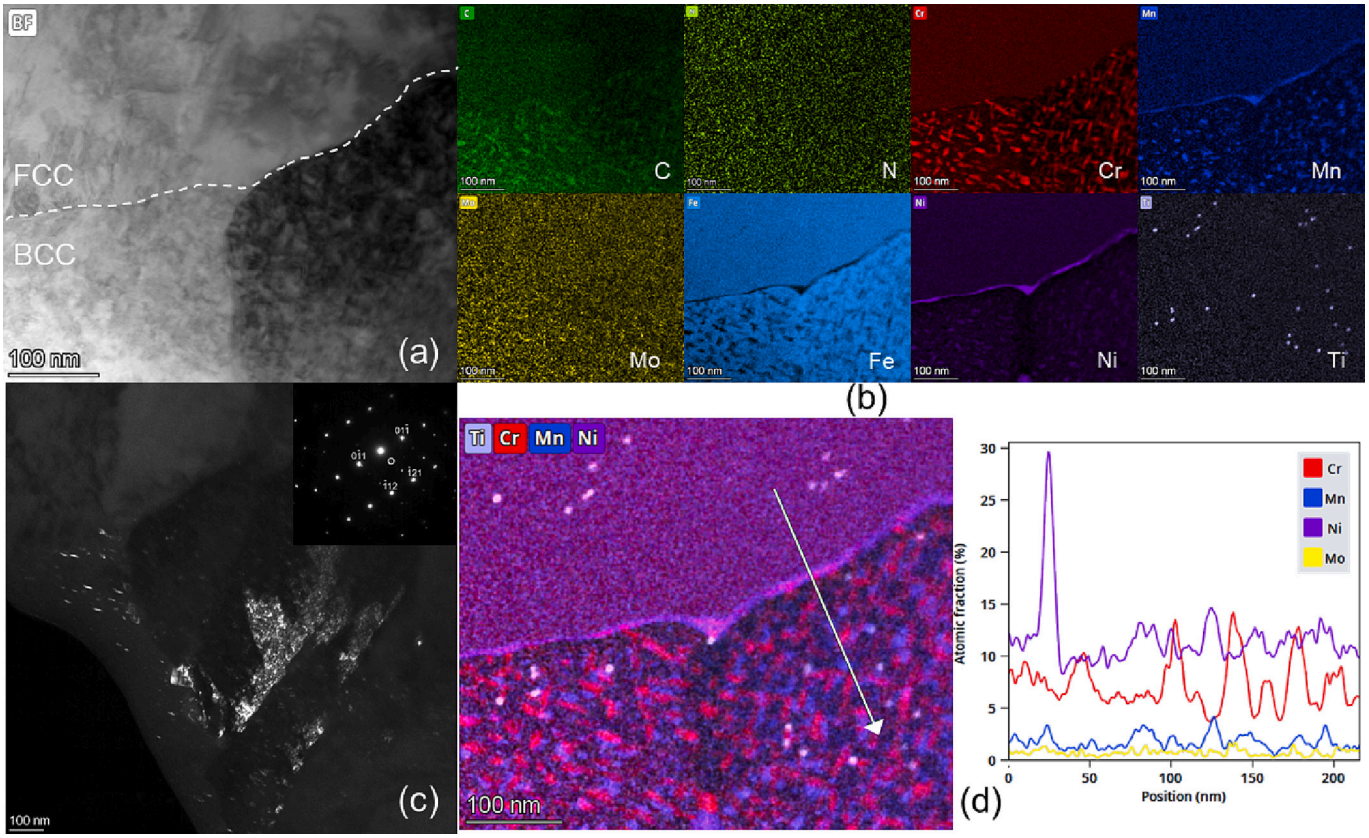

Fig. 7. Nano-carbides at the FB in the NG TA material. (a) STEM-BF image and (b) the corresponding elemental map; (c) TEM DF with nano-carbides' reflection from SAED pattern along zone axis [113]; (d) The color-mixed elemental map and extracted profile with line position indicated in the map.

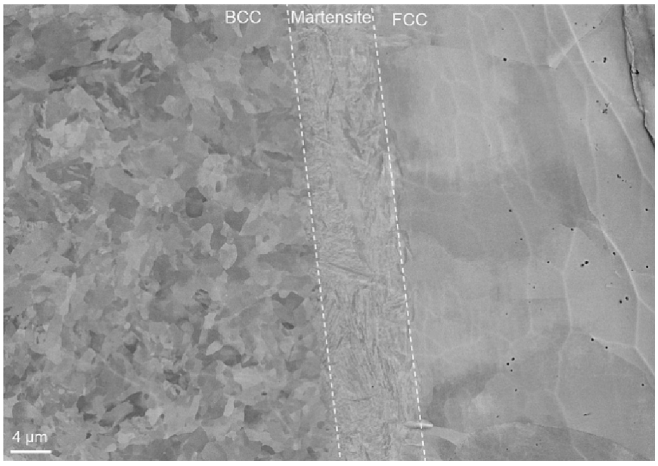

Fig. 8. The NG TA material contains a martensite area between the FCC (right) phase and BCC phase with a width of about 11 μm.

Fourier transform (FFT), which can be indexed with Mo_2C crystal of orthorhombic lattice along the [110] zone axis.

3.5. WAXS of carbides in the HAZ

The Rietveld refinement results of WAXS patterns are presented in Fig. 17. The X-ray diffraction pattern confirms the two types of carbides observed in TEM, M_3C and Mo_2C. The AR and TA patterns are quite similar in general and contain approximately 2% carbides. However, the TA pattern shows slightly larger volume fraction of carbides than the AR pattern. After thermal aging the ratio of M_3C carbides increased in the NG TA material compared to the NG AR material. In TEM observations of the TA material, there is a higher amount of Mo_2C carbides than in the AR material, but WAXS refinement has shown slightly higher Mo_2C fraction in the AR material. The controversy results are mainly because the nano-sized Mo_2C has weak broad peaks and its fraction is at the detection limit of WAXS.

3.6. APT analysis

The effect of thermal aging on the potential P segregation in the LAS HAZ was studied with APT. Comparing the P content on grain boundaries using APT is a challenging task, as the APT data is very local with a small analysis volume. Analyzing a specific grain boundary is not enough, as different types of grain boundaries often contain different amounts of segregation [28]. Thus, a full characterization of the type of grain boundary (including electron backscatter diffraction and transmission Kikuchi diffraction) would be needed, and a large number of grain boundaries need to be analyzed in order to get a statistically significant result. This approach is thus very time consuming and work intense. In this paper, another path was chosen. This was to compare the average amount of the element concentration in the interior of the HAZ grains from multiple APT samples. If the segregation after thermal aging is strong enough, the bulk P content in the interior of the grains would be lower in the NG TA material than in the NG AR material.

The APT analyses of the HAZ bulk of the AR and TA materials contained no grain boundaries. The average bulk compositions measured from multiple APT analyses can be seen in Table 3. The P contents are low, 50 ± 20 at.ppm and 40 ± 20 at.ppm in the AR and TA materials, respectively. Though the bulk P content in the interior of the HAZ grains are slightly lower in the NG TA material than in the NG AR material, there is no evidence of a significant P segregation to grain boundaries from thermal aging.

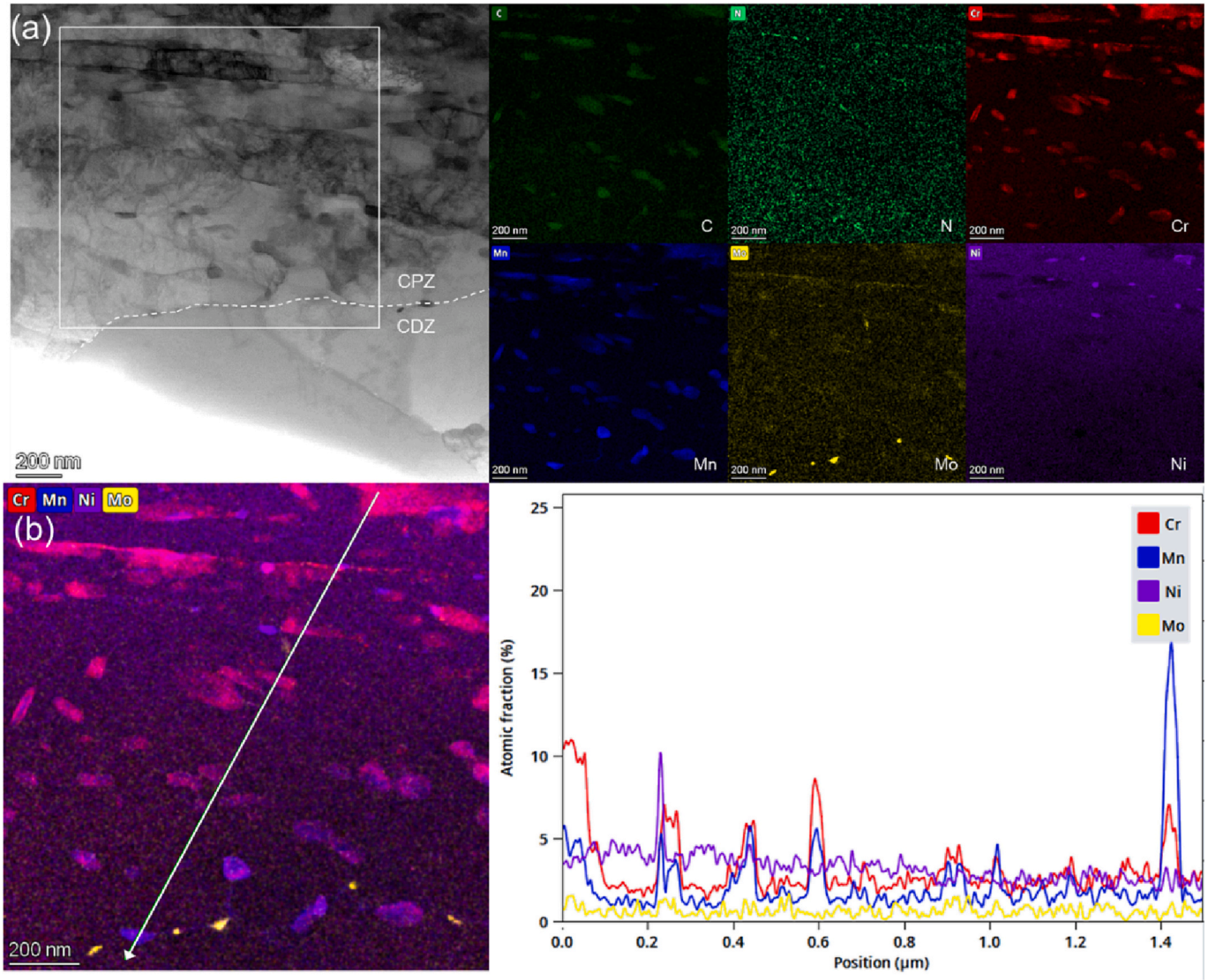

Fig. 9. Carbides at the interface of the CPZ and CDZ in the NG TA material. (a) STEM BF image and corresponding elemental map of framed area in BF image. (b) Combined Cr, Mn, Ni and Mo maps and extracted profile for the line indicated in color-mixed image.

In Fig. 18, representative reconstructions of AR and TA materials are shown. In these analyses, occasional dislocation lines are present. These can be observed by APT due to the enrichment of Mo, Mn and C. Statistically, there is also a small tendency for P to segregate to these dislocation lines. However, no difference in P segregation to dislocation lines between the NG AR and TA materials could be proven by the APT measurements.

In the NG AR material, a part of a carbide was analyzed by APT. The carbide contains mainly Fe (59 at.%) and Mn (14 at.%) as metallic elements. Mo and Cr were also enriched in the carbide (both by <2 at.% each). The C content was measured to be 24 at.%, but might be slightly underestimated due to cascades of C atoms evaporating simultaneously during APT analysis and detector deadtime [29]. In connection to this carbide, a low-angle boundary enriched in C and P is observed. This shows that there is probably a certain level of P segregation on boundaries already before long-term thermal aging. The bulk P content is around 90 at.ppm (50 wt.ppm), see Table 2, so the APT measurements suggest that about half of the P is segregated already before aging.

4. Discussion

The microstructure and carbide size distribution from different regions in LAS of the NG AR and NG TA materials are summarized in Table 4. At the FB, nanometer-sized precipitates were observed. In the NG TA material these are nano-carbides. However, in the NG AR material, the majority of the nano-precipitates at the FB (tens of nanometers wide zone) are nitrides whereas nano-carbides dominate in regions slightly further away from the FB. These nano-carbides at the FB of the NG TA material have a perfect Bargaryatskii's orientation relationship with the BCC matrix, which is reported for the first time in a DMW, according to the knowledge of the authors. The orientation relationship between nanometer-sized carbides with the BCC matrix indicates that they precipitated directly on the crystal defects of ferrite matrix during PWHT.

Long-term thermal aging triples the width of the CPZ. In the CPZ, the number of carbides is much lower and the size of the carbides is also smaller in the AR material than in the TA material. This is in line with the result that the long-term thermal aging increases the microhardness peak close to the FB. Except nano-sized nitrides/carbides at the FB, the dominant carbides in the CPZ are $(Fe, Cr, Mn)_3C$ with size about 50–100 and 100–200 nm in the NG AR and NG TA materials, respectively. The CPZ contains the highest density of intergranular and intragranular $(Fe, Cr, Mn)_3C$ carbides in all regions of the LAS side. Even though $(Fe, Cr, Mn)_3C$ carbides also contain a small amount of Mo, the Mo_2C carbides

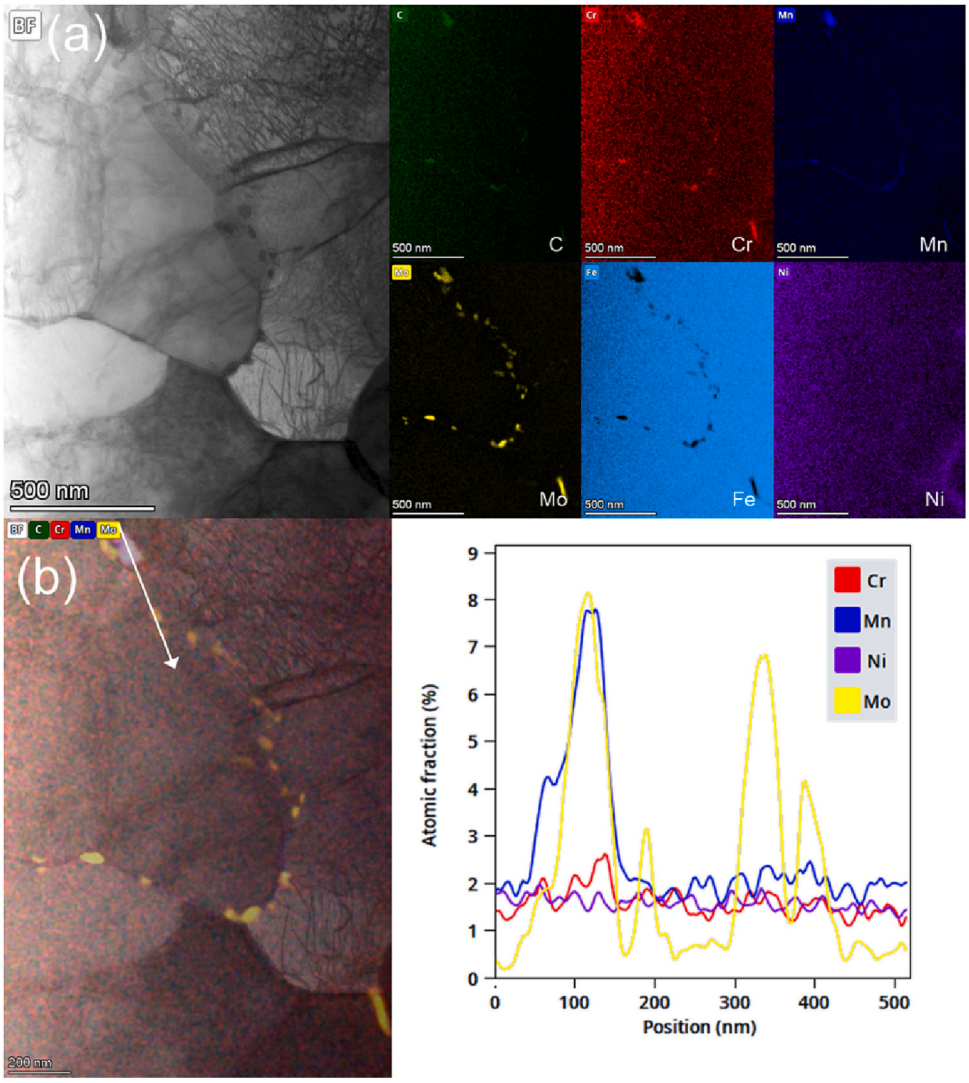

Fig. 10. Carbides in the CDZ in the NG AR material. (a) STEM BF image and corresponding elemental maps; (b) Mixed of BF image and C, Cr, Mn, and Mo elemental maps and the extracted profile from line marked in the mixed image.

population is very small in the CPZ. It is interesting to note that Mo_2C carbides are frequently observed at the interface between the CPZ and CDZ. These features of CPZ are common in both the AR and TA materials even when a wide CPZ was formed associated with a tempered martensite type of FB. The columnar grains in the narrow CPZ are similar to the lath grains in the tempered martensite since they may be formed with the same mechanism resulting from high cooling rate at FB.

Long-term thermal aging slightly reduces the width of the CDZ. This indicates a continuous diffusion of carbon from the CDZ to the CPZ during thermal aging. The grain size is much smaller and the dislocation density is higher in the CPZ than in the CDZ. The carbide population is the smallest in the CDZ compared to the CPZ and the HAZ. Only small-sized Mo_2C carbides decorating mainly the grain boundaries can be found in the CDZ. Occasionally, few $(Fe, Mn, Cr)_3C$ carbides can be found at grain boundaries too. In the CDZ, $(Fe, Mn, Cr)_3C$ carbides contain higher Mn content than Cr, which is different to the CPZ where $(Fe, Cr, Mn)_3C$ were formed with higher Cr content than Mn.

The carbide density in the HAZ is evidently higher than in the CDZ but lower than in the CPZ. In the LAS HAZ, carbides were identified as $(Fe, Mn, Cr)_3C$ and Mo_2C. Long-term thermal aging coarsens the carbides size in the HAZ (up to a magnitude longer), which corresponds well to the WAXS measurement in the HAZ where higher percentage of carbides was observed in the TA than the AR material. The fraction of carbide-free grains in the HAZ is 2–3 times higher in the NG TA material than in the NG AR material. These grains devoid of visible carbides are formed likely during phase transformation where C partitioning occurred.

The welding technique (*e.g.,* NG or buttering) has a significant effect on the solidification, cooling rate, internal stresses and mixing of metals, impacting the forming solidification microstructure and the carbides at the FB in a DMW [30] [31]. However, the data on the microstructural changes and carbide formation in plant-relevant NG DMW occurring upon post-weld heat treatment and long-term thermal aging is very limited. The microstructure and carbides in the FB and HAZ regions have a direct influence on the local brittle fracture behavior and on the cracking susceptibility of a DMW [13]. During long-term thermal aging in the NG mock-up, more carbon from the LAS side can diffuse from the CDZ to the FB [1]. As shown in this work, long-term thermal aging leads to moderate changes in the microstructure and carbides in the FB, CPZ, CDZ and HAZ regions in the NG DMW. The peak hardness of the NG DMW was reported to coincide with the position of carbon peak values [3] [5], which is in line with the microhardness measurement carried out at two different loads and the quantitative analysis of C concentration across the FB by WDS. In this work higher microhardness peak closer to the FB and wider CPZ/narrower CDZ in the TA material were observed. Ahonen et al. [5] reported a lower microhardness after

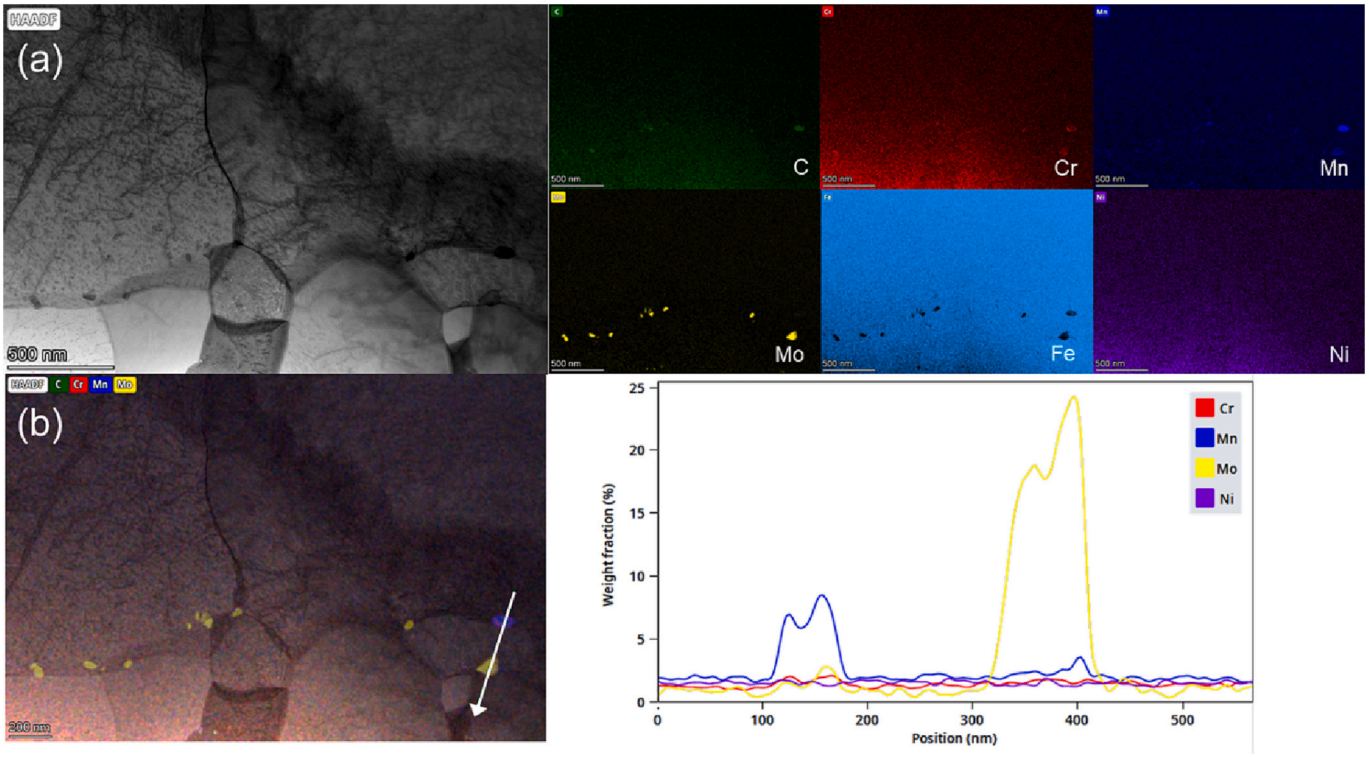

Fig. 11. Carbides in the CDZ of the NG TA material. (a) STEM BF image and corresponding elemental maps; (b) Mix of BF image and C, Cr, Mn, and Mo elemental maps and the line profile from the arrow line in the mixed image.

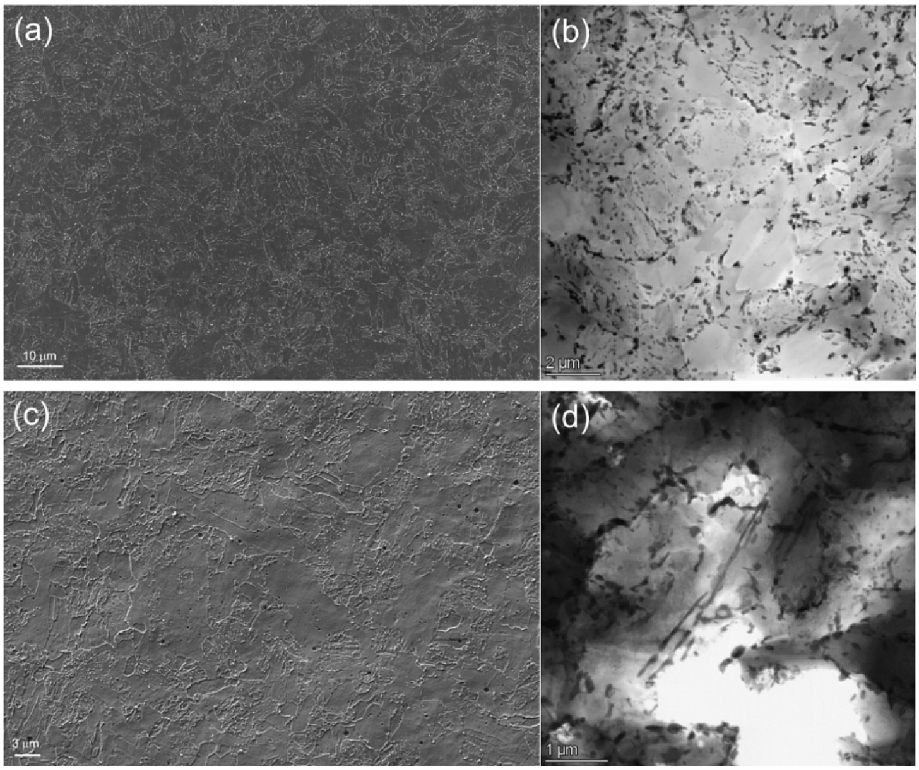

Fig. 12. Microstructure and carbide distribution in the HAZ of (a-b) the NG AR and (c-d) the TA material. (a,c) SEM SE images and (b,d) STEM BF images.

thermal aging. However, the difference in the peak hardness mainly derives from the indentation parameters particular the spacing between the first indents to the FB.

Nevasmaa et al. [32] reported that a decrease in fracture resistance of DMW can stem from increased metallurgical constraint and crack (growth) driving force accentuated by the high, local mismatch state, coupled with inherent local inhomogeneity of the near-interface regions. Under high local strength mismatch, the inherent strength and

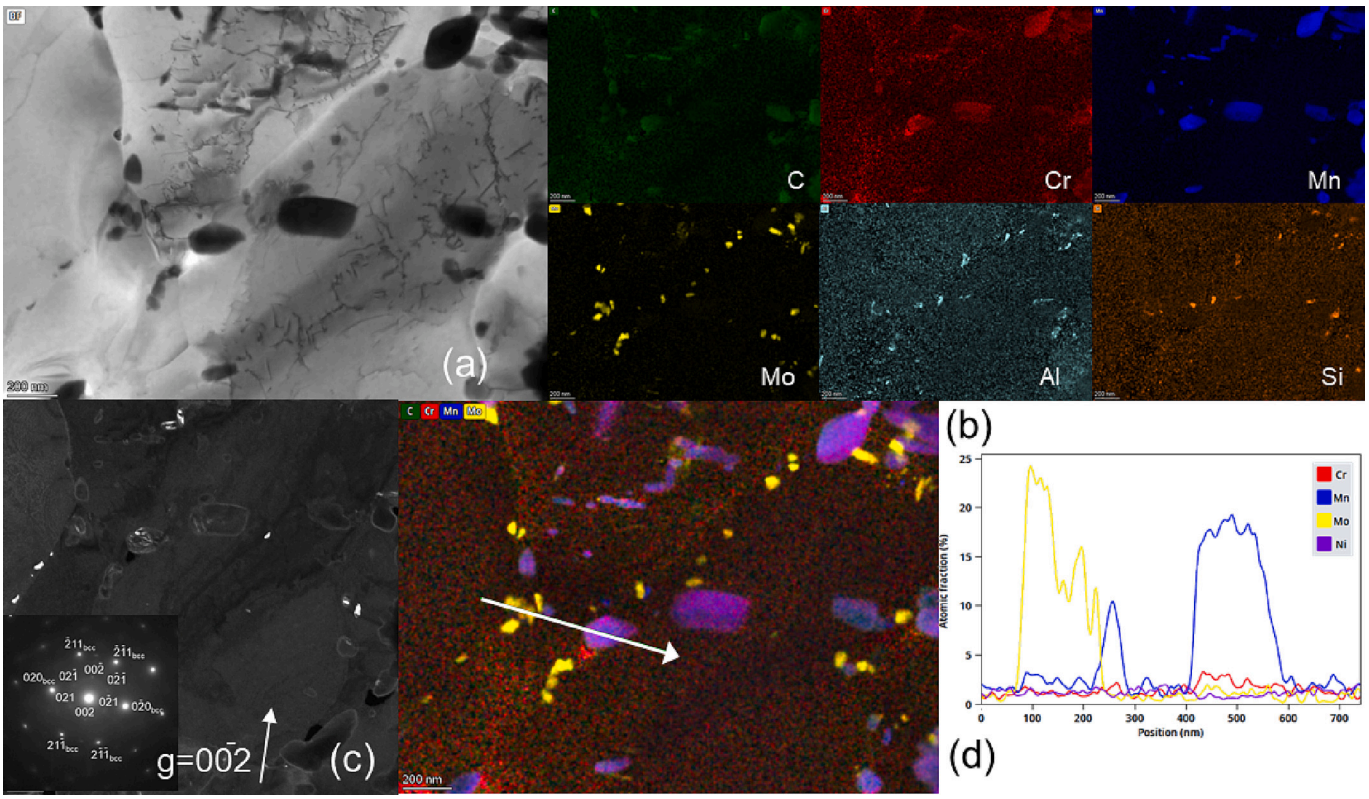

Fig. 13. Carbides in the HAZ of the NG AR material. (a-b) STEM-BF image and selected elemental maps; (c) TEM DF image from Mo_2C's reflection $00\bar{2}$ with the inset SAED pattern indexed with BCC zone axis [102] and Mo_2C zone axis [100]; (d) Mix of selected elemental maps and extracted line profile.

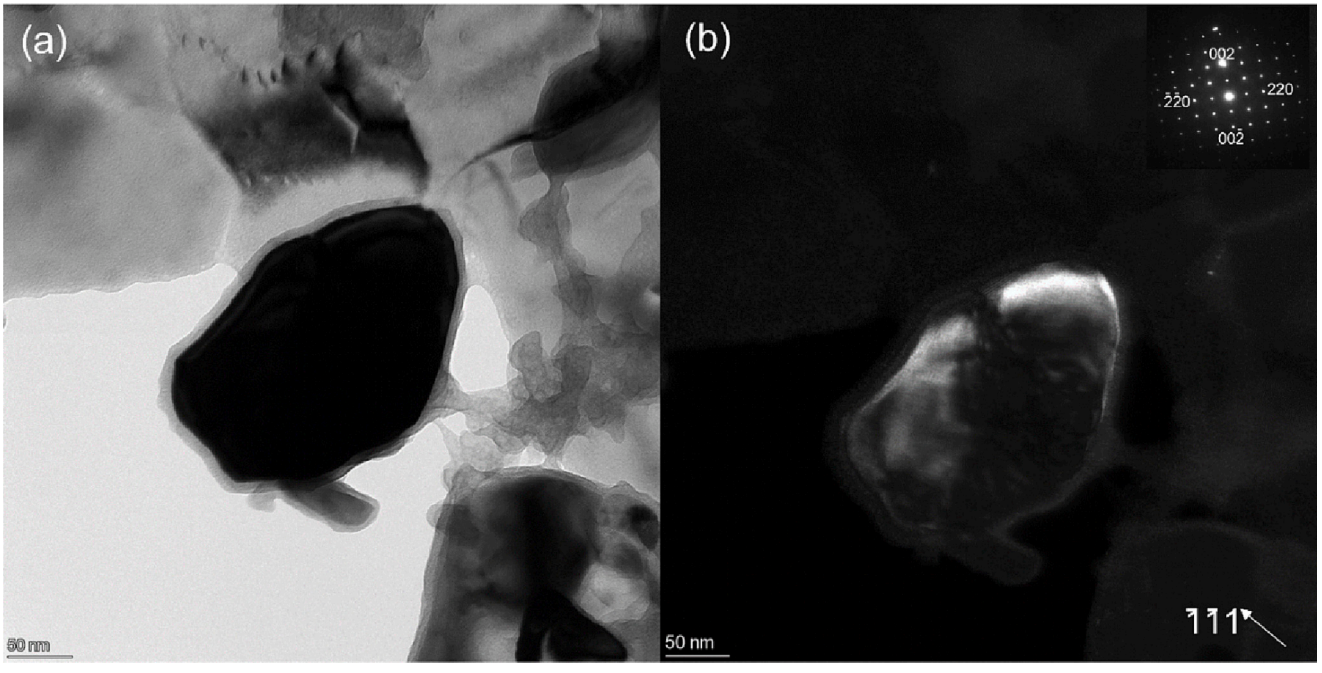

Fig. 14. TEM BF image (a) and DF image (b) along the [$11\bar{2}0$] zone axis in the HAZ of the NG AR sample with the inset being the SAED pattern.

toughness properties of two neighboring, mismatching microstructures become increasingly important, which may, in some cases, dictate the entire fracture behavior of a DMW. As observed in this study, long-term thermal aging results in higher microhardness mismatch at the FB, larger/denser carbides in the CPZ and longer carbides and higher fraction of carbide-free grains in the HAZ, which may lead to the formation of local brittle zones and can cause low fracture toughness. The brittle fracture behavior of the same mock-up studied in this paper was recently reported by Lindqvist et al. [22]. It was found that for four T_0 fracture toughness specimens aged at 400 °C for 15,000 h, the crack initiation and propagation occur only in the HAZ without deviating to the FB, leading to a much lower (~1/3) average fracture toughness compared to

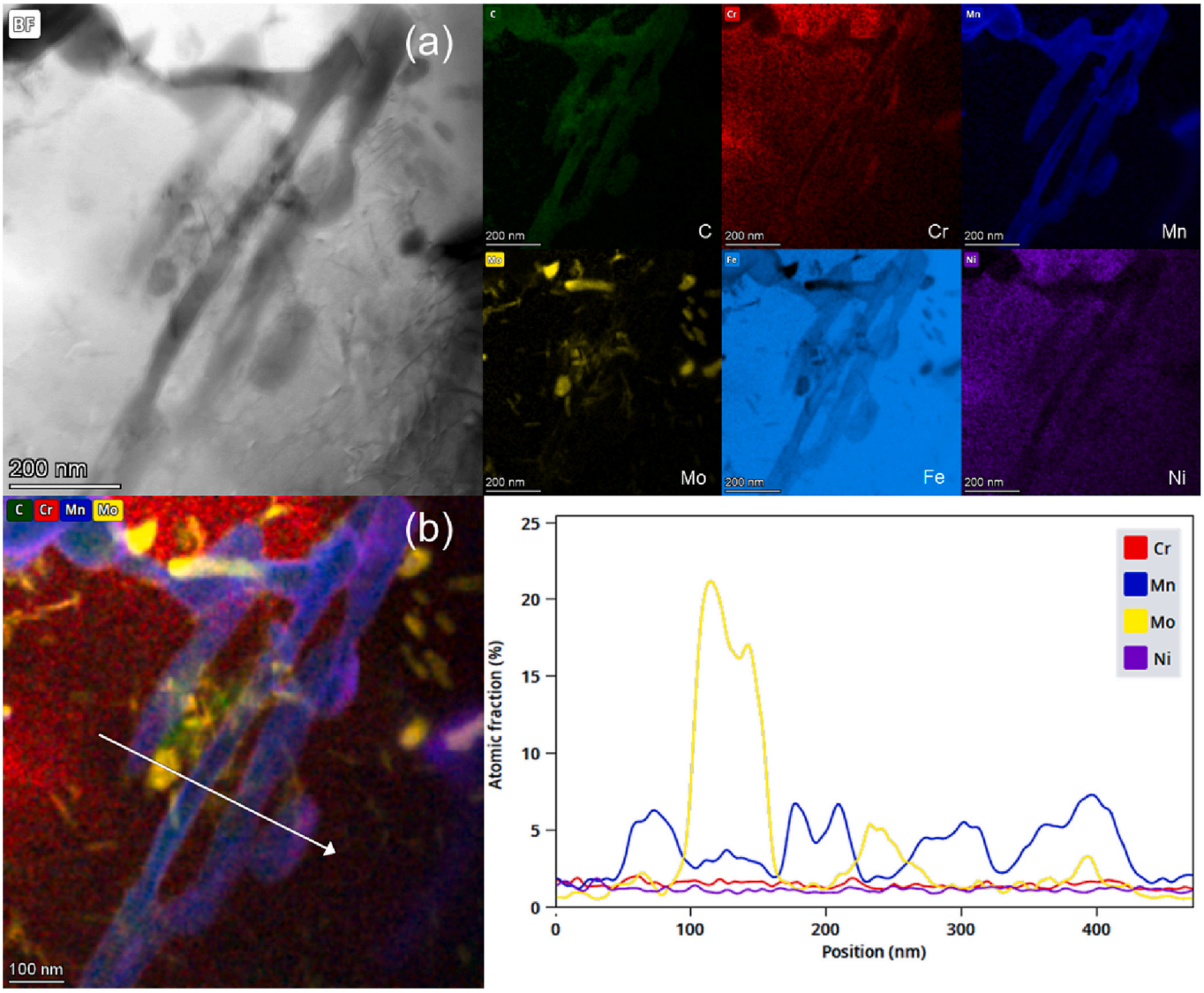

Fig. 15. Carbides in the HAZ of the NG TA material. (a) STEM-BF image of carbides and corresponding selected elemental maps; (b) combined elemental map and extracted line profile from the line position indicated in the image.

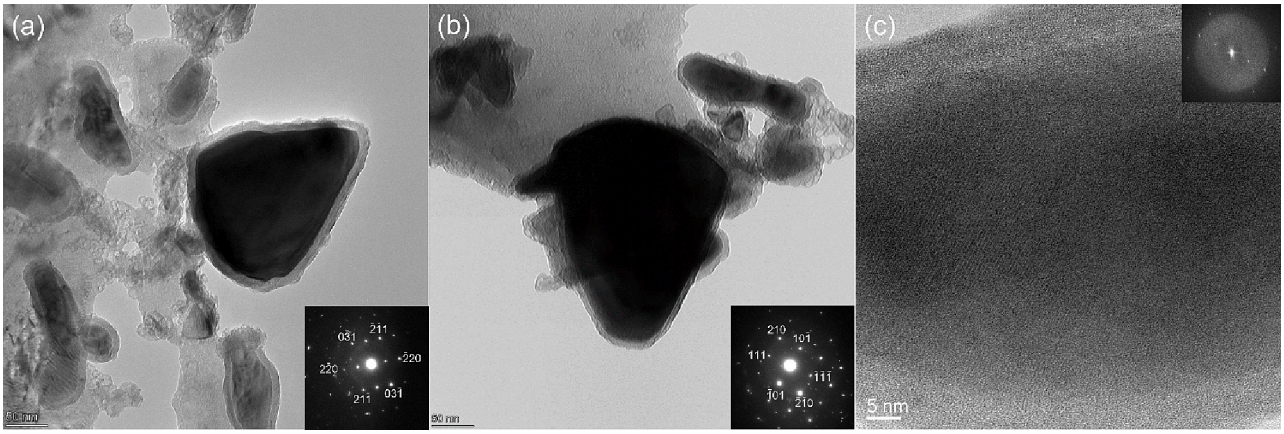

Fig. 16. TEM image of Fe carbides and Mo carbides in the HAZ of the NG TA sample. (a) TEM BF image of Fe carbide along the [113] zone axis; (b) TEM BF image of Fe carbides along [12$\bar{1}$1]; (c) HRTEM of a Mo carbide with the inset of its FFT, which fits to zone axis [110].

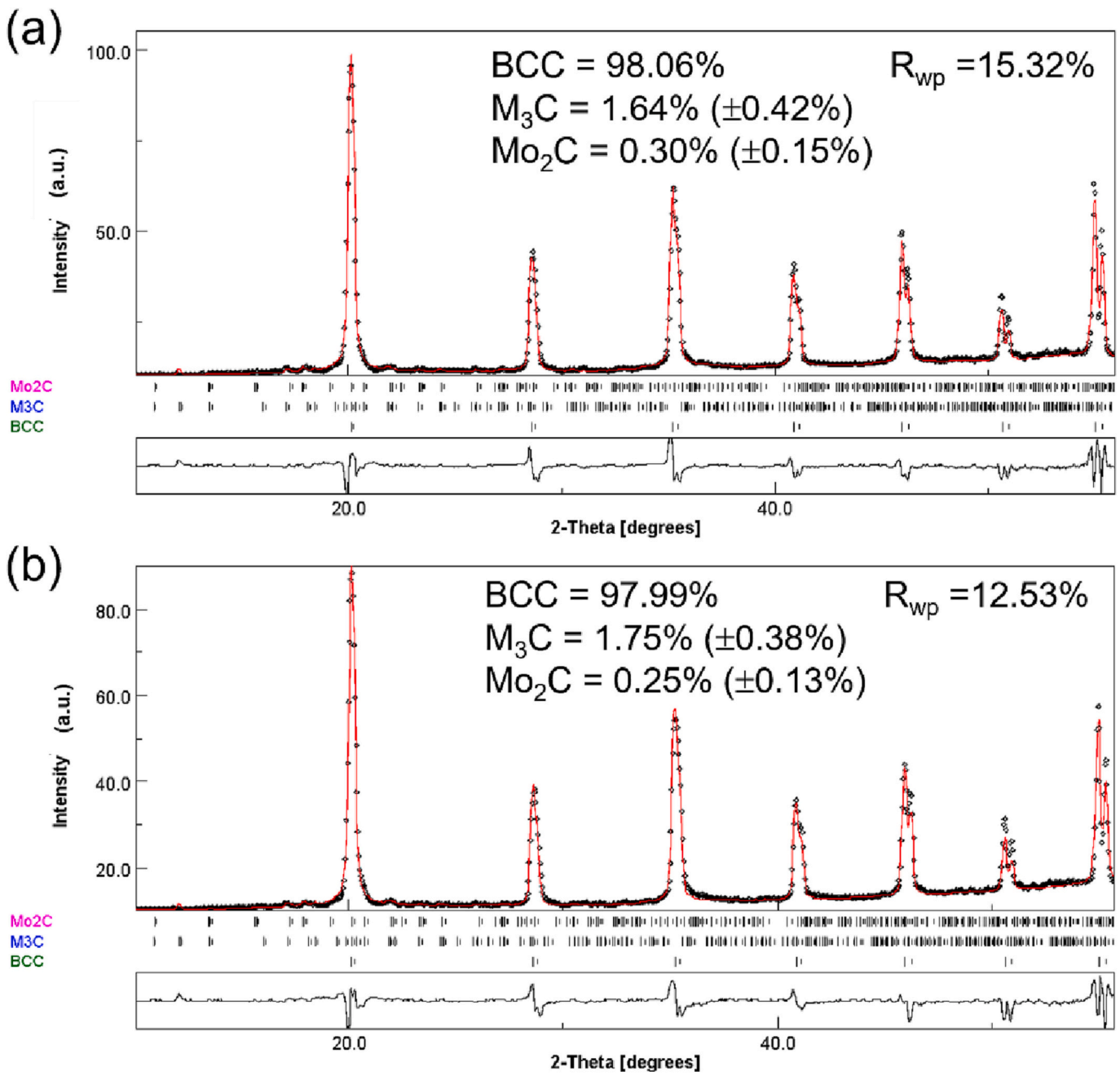

Fig. 17. WAXS patterns of (a) the NG AR material and (b) NG TA material.

the other specimens with the notch crack placed in the CDZ and the crack path deviation to the FB. The thermal aging and the resultant formation of local brittle zones, *e.g.* coarsening carbides and higher fraction of carbide-free grains in the HAZ may contribute to the observed low fracture toughness.

The APT results suggest that in the studied DMW mock-up with low bulk phosphorus no significant phosphorus segregation was observed and about half of the phosphorus is segregated already before aging. Though a slightly higher amount of grain boundary cracking has been seen in the master curve test specimens after thermal aging, which can be assumed to be due to phosphorus segregation, the amount of phosphorus segregation is not significant, as is the shift in T_0 [22] [23], which is in line with the APT results in this paper. Moreover, the thermal aging at 400 °C for 15,000 h results in a lower shift of T_0 than that of impact toughness. Therefore, the thermal aging and the resultant microstructural changes and carbides formation affect more the crack arrest and propagation mechanism than the initiation mechanism.

In the majority of the DMW literature, the carbides were referred to as chromium carbide precipitates without detailed information of the chemistry and crystal structure or indexed as $Cr_{23}C_6$ [3] [12] [19] [33]. Choi et al. [12] reported that $Cr_{23}C_6$ precipitated at the FB immediately after DMW welding and the number of $Cr_{23}C_6$ precipitates in the FB regions increased after thermal aging for 1713 h at 400 °C. However, the number of precipitates decreased by the coarsening and coalescence of precipitates with a thermal aging of 3427 h. In this paper, thermal aging at 400 °C for 15,000 h results in both a number increase and coarsening of precipitates at the FB, CPZ and HAZ. This will result in an increase of contact surface between the LAS (anode) and Cr-rich precipitates (cathode) and then cause the increase of the corrosion rate if the DMW is exposed to high-temperature water. In the present study the dominant carbides are M_3C θ carbides verified by index under multiple zone axes and $M_{23}C_6$ was not detected in any of our TEM samples. One possible

Table 3
Compositions of the interior of the grains in the HAZ of the NG AR and TA materials from APT. The error given is the standard deviation between the APT runs used, indicating small local differences in the composition, resolved by APT.

	TVO AR	TVO TA
	At.%	At.%
Fe	Bal.	Bal.
Mn	1.08 ± 0.24	1.11 ± 0.44
Ni	0.79 ± 0.04	0.76 ± 0.02
Si	0.42 ± 0.02	0.42 ± 0.01
Mo	0.22 ± 0.04	0.19 ± 0.10
Cr	0.23 ± 0.08	0.22 ± 0.04
Cu	0.035 ± 0.003	0.034 ± 0.005
N	0.03 ± 0.04	0.05 ± 0.01
Co	0.02 ± 0.01	0.01 ± 0.01
C	0.16 ± 0.18	0.04 ± 0.04
Al	0.005 ± 0.003	0.020 ± 0.019
P	0.005 ± 0.002	0.004 ± 0.002
V	0.002 ± 0.001	0.002 ± 0.002

reason is that the chemical composition, cooling rate, temperature gradient and PWHT affect the FB carbide type. Another reason can be due to the similarity of a few high index zone axes in electron diffraction patterns with the minor differences in closed pack plane distance between BCC and FCC lattice at the FB, which may have caused misindexation in literatures.

5. Conclusions

The microstructure and carbides' crystal structure, chemistry, morphology and size in the FB and the LAS HAZ were analyzed for the NG SA508/Alloy 52 DMW mock-up, which is fully representative of an actual nuclear component. Based on the obtained results, the following conclusions can be drawn:

- The nanometer-sized precipitates at the FB are nano-carbides in the NG TA material and nano-nitrides in the NG AR material. These Cr/Mn-rich carbides at the FB have a fixed Bagaryatskii orientation relationship with the BCC matrix, which is reported for the first time in a DMW.
- Long-term thermal aging increases the microhardness peak (~20 HV) close to the FB and triples the width of the CPZ. In the CPZ, the number of carbides is much lower and the size of the carbides is smaller in the AR material than in the TA material.
- The dominant carbides are (Fe, Cr, Mn)$_3$C in the CPZ but (Fe, Mn, Cr)$_3$C in the CDZ and the HAZ. These carbides are M$_3$C θ carbides.
- Long-term thermal aging coarsens the carbide size in the HAZ. The length of the carbide can be a magnitude longer after aging. The fraction of grains devoid of visible carbides in the HAZ is 2–3 times higher in the NG TA material than in the NG AR material.
- After thermal aging, the higher microhardness mismatch at the FB, the larger/denser carbides in the CPZ and the coarsened carbides and higher fraction of carbide-free grains in the HAZ may lead to local brittle zones and could cause low fracture toughness.
- There is no evidence of a significant phosphorus segregation to grain boundaries in HAZ due to thermal aging.

Declaration of Competing Interest

The authors declare that they have no known competing financial interests or personal relationships that could have appeared to influence the work reported in this paper.

Table 4
Summary of grain size and carbide distribution in LAS of AR and TA materials.

		CPZ	CDZ	HAZ
Zone width	AR	≤500 nm ≥1500 nm	50 μm	N/A
	TA	Or ~ 11 μm (tempered martensite FB)	40 μm	N/A
Grain size	AR	100–300 nm	4.2 μm	1.2 μm
	TA	100–300 nm	4.0 μm	1.4 μm
Carbide type and size	AR	Nano-sized nitrides: ≤10 nm; (Fe, Cr, Mn)$_3$C: ≤100 nm	Mo_2C: ≤40 nm; (Fe, Mn, Cr)$_3$C: ≤150 nm	(Fe, Mn, Cr)$_3$C: ≤300 nm; Mo_2C: ≤100 nm
	TA	Nano-sized carbides: ≤20 nm; (Fe, Cr, Mn)$_3$C: ≤200 nm	Mo_2C: ≤80 nm; (Fe, Mn, Cr)$_3$C: ≤150 nm	(Fe, Mn, Cr)$_3$C: ≤2 μm (fiber) Or ≤ 300 nm (round); Mo_2C: ≤100 nm
Carbide density	AR	Higher than in HAZ	Much lower than in HAZ	Similar to normal reactor pressure vessel steel
	TA	Higher than AR	Similar to AR	Higher than AR

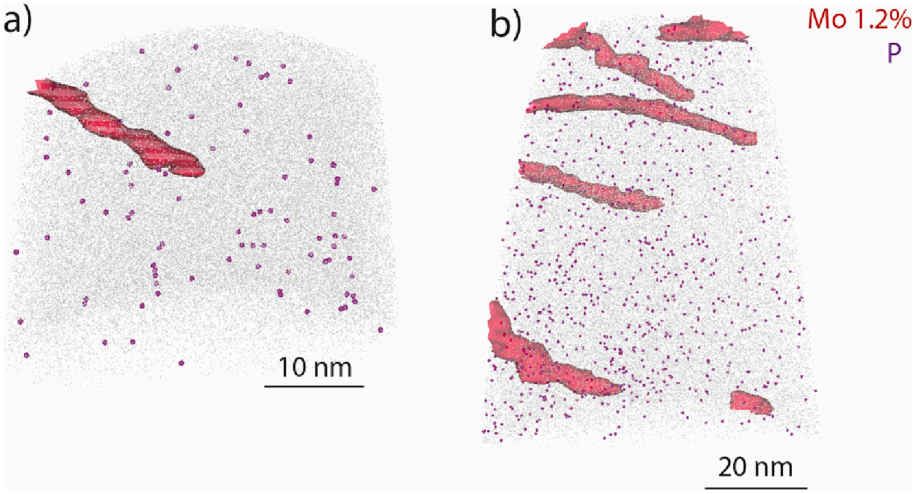

Fig. 18. APT reconstructions of (a) NG AR and (b) NG TA material. Purple dots correspond to P atoms, and red surfaces to 1.2% Mo (isoconcentration surfaces), delineating Mo enrichment at dislocations. Grey shows the extent of the analyses. (For interpretation of the references to color in this figure legend, the reader is referred to the web version of this article.)

Data availability

The data that support the findings of this study are available from the corresponding author upon reasonable request.

Acknowledgements

The authors wish to express their gratitude for the funding and support from Ringhals AB, OKG AB, Teollisuuden Voima Oyj and VTT Technical Research Centre of Finland within the FEMMA (Forum for the Effect of Thermal Aging and Microstructure on Mechanical and EAC Behavior of Ni-based Alloy Dissimilar Metal Welds) research project. The authors also thank NKS for funding the NKS-FEMMA (AFT/NKS-R (22)134/4) project. The authors would like to thank P. Arffman, J. Lydman, J. Lukin and L. Sirkiä for the experimental contributions. The authors would like to thank U. Ehrnstén, P. Efsing, B. Forssgren, H. Reinvall and H. Hänninen for suggestions and discussions. The authors acknowledge the provision of facilities and technical support by Aalto University at OtaNano - Nanomicroscopy Center (Aalto-NMC). The APT experiments were performed at Chalmers Materials Analysis Laboratory (CMAL).

References

[1] M. Ahonen, S. Lindqvist, T. Sarikka, R. Mouginot, E. Leskelä, J. Lydman, U. Ehrnstén, P. Nevasmaa, T. Seppänen, P. Arffman, H. Hänninen, Thermal ageing and mechanical performance of narrow-gap dissimilar metal welds, VTT Technol. 333 (2018).
[2] W.-C. Chung, J.-Y. Huang, L.-W. Tsay, C. Chen, Microstructure and stress corrosion cracking behaviour of the weld metal in alloy 52-A508 dissimilar welds, Mater. Trans. 52 (1) (2011) 12–19.
[3] A. Akhatova, F. Robaut, M. Verdier, M. Yescas, F. Roch, C. Tassin, H. Landeghem, Microstructural and mechanical investigation of the near fusion boundary region in thermally aged 18MND5 / alloy 52 narrow-gap dissimilar metal weld, Mater. Sci. & Eng. A 788 (139592) (2020).
[4] Z. Chen, Y. Lu, TEM observation of Martensite layer at the weld Interface of an A508III to Inconel 82 dissimilar metal weld joint, Metall. Mater. Trans. A 46A (2015) 5494–5498.
[5] M. Ahonen, R. Mouginot, T. Sarikka, S. Lindqvist, Z. Que, U. Ehrnstén, I. Virkkunen, H. Hänninen, Effect of thermal ageing at 400°C on the microstructure of ferrite-austenite interface of nickel-base alloy narrow-gap dissimilar metal weld, Metals 10 (3) (2020) 421.
[6] J. Parker, G. Stratford, Characterisation of microstructures in nickel based transition joints, J. Mater. Sci. 35 (2000) 4099–4107.
[7] J. Hou, Q. Peng, Y. Takeda, J. Kuniya, T. Shoji, J. Wang, E.-H. Han, W. Ke, Microstructure and mechanical property of the fusion boundary region in an alloy 182-low alloy steel dissimilar weld joint, J. Mater. Sci. 45 (2010) 5332–5338.
[8] P. Efsing, B. Forssgren, R. Kilian, Root cause failure analysis of defected J-groove welds in steam generator drainage nozzles, in: Proceedings of the Twelfth International Conference on Environmental Degradation of Materials in Nuclear Power Systems-Water Reactors, 2005.
[9] A. Jenssen, K. Norrgard, J. Lagerstrom, G. Embring, C. Jansson, P. Efsing, Structural assessment of defected nozzle to safe-end welds in Ringhals-3 and -4, in: Proc. Fontevraud V Intl. Symp, 2000.
[10] P. Efsing, J. Lagerström, Analysis of a defected dissimilar metal weld in a PWR power plant, in: 10th Int Conf Nucl Eng, 2002.
[11] Z. Que, M. Lindroos, J. Lydman, N. Hytönen, S. Lindqvist, P. Efsing, P. Nevasmaa, P. Arffman, Brittle fracture initiation in decommissioned boiling water reactor pressure vessel head weld, J. Nucl. Mater. 569 (153925) (2022).
[12] K. Choi, S. Yoo, S. Kim, T. Kim, J. Ham, J. Lee, J. Kim, Microstructural evolution and corrosion behaviour of thermally aged dissimilar metal welds of low-alloy steel and nickel-based alloy, Corros. Sci. 153 (2019) 138–149.
[13] H. Wang, G. Wang, F. Xuan, C. Liu, S. Tu, Local mechanical properties of a dissimilar metal welded joint in nuclear power systems, Mater. Sci. & Eng. A 568 (2013) 108–117.
[14] S. Yoo, K. Choi, C. Bahn, S. Ki, J. Kim, J. Kim, Effects of thermal aging on the microstructure of type-II boundaries in dissimilar metal weld joints, J. Nucl. Mater. 459 (2015) 5–12.
[15] A. Blouin, S. Chapuliot, S. Marie, C. Niclaeys, J. Bergheau, Brittle fracture analysis of dissimilar metal welds, Eng. Fract. Mech. 131 (2014) 58–73.
[16] J. Gao, J. Tan, M. Jiao, X. Wu, L. Tang, Y. Huang, Role of welding residual strain and ductility dip cracking on corrosion fatigue behavior of alloy 52/52M dissimilar metal weld in borated and lithiated high-temperature water, J. Mater. Sci. Technol. 42 (2020) 163–174.
[17] J. Kim, K. Choi, C. Bahn, K. J.H, In situ Raman spectroscopic analysis of surface oxide films on Ni-base alloy/low alloy steel dissimilar metal weld interfaces in high-temperature water, J. Nucl. Mater. 449 (2014) 181–187.
[18] H. Ming, J. Wang, E. Han, Comparative study of microstructure and properties of low-alloy-steel/nickel-based-alloy interfaces in dissimilar metal weld joints prepared by different GTAW methods, Mater. Charact. 139 (2018) 186–196.
[19] P. Joly, M. Yescas, E. Keim, Fracture toughness in the ductile-brittle transition and thermal ageing behavior of decarburized heat affected zone of Alloy 52 dissimilar metal welds of nuclear components, in: Proceedings of the ASME-2014 Pressure Vessel and Piping Conference, Anaheim, California, USA, 2014.
[20] R. Mouginot, Effect of Thermal Ageing on Alloys 690 and 52 in Pressurized Water Reactor Applications, Doctoral dissertation,, Aalto University, 2017.
[21] H. Wang, G. Wang, F. Xuan, S. Tu, Fracture mechanism of a dissimilar metal welded joint in nuclear power plant, Eng. Fail. Anal. 28 (2013) 134–148.
[22] S. Lindqvist, Z. Que, P. Nevasmaa, N. Hytönen, The effect of thermal aging on fracture properties of a narrow-gap alloy 52 dissimilar metal weld, Eng. Fract. Mech. 281 (109056) (2023).
[23] S. Lindqvist, N. Hytönen, L. Sirkiä, P. Arffman, J. Lydman, Y. Ge, P. Nevasmaa, Z. Que, Fracture in the Ductile-To-Brittle Transition Region of A Narrow-Gap Alloy 52 and Alloy 52 Dissimilar Metal Weld With Buttering, in: ASME PVP2022–80690, Las Vegas, USA, 2022.
[24] N. Hytönen, Y. Ge, Z. Que, S. Lindqvist, P. Nevasmaa, I. Virkkunen, P. Efsing, Study of fusion boundary microstructure and local mismatch of SA508/alloy 52 dissimilar metal weld, J. Nucl. Mater. (2023).
[25] N. Hytönen, Y. Ge, Z. Que, S. Lindqvist, J. Lydman, U. Ehrnstén, P. Rautala, I. Virkkunen, P. Efsing, Effect of Microstructure on Mechanical Behavior of Ni-base Alloy Dissimilar Metal Welds, in: The 20th International Conference on Environmental Degradation of Materials in Nuclear Power Systems-Water Reactor Meeting, Colorado, USA, 2022.
[26] L. Lutterotti, Maud: a Rietveld analysis program designed for the internet and experiment integration, Acta Crystallogr. A: Found. Crystallogr. 56 (s1) (2000) 54.
[27] Y. Bagaryatskii, Veroyatnue mechanezm raspada martenseeta, Dokl. Akad. Nauk SSSR 73 (1950) 1161.
[28] L. Zhang, B. Radiguet, P. Todeschini, C. Domain, Y. Shen, P. Pareige, Investigation of solute segregation behavior using a correlative EBSD/TKD/APT methodology in a 16MND5 weld, J. Nucl. Mater. 523 (2019) 434–443.
[29] M. Thuvander, J. Weidow, J. Angseryd, L. Falk, F. Liu, M. Sonestedt, K. Stiller, H. Andren, Quantitative atom probe analysis of carbides, Ultramicroscopy 111 (6) (2011).
[30] S. Kou, Welding Metallurgy, 2nd edition, John Wiely & Sons, Inc., 2003.
[31] N. Hytönen, Z. Que, S. Lindqvist, J. Lydman, Y. Ge, I. Virkkunen, U. Ehrnstén, P. Rautala, P. Efsing, B. Forssgren, Fusion boundary microstructure and fracture behaviour of a narrow-gap Alloy 52 dissimilar metal weld and an Alloy 52 dissimilar metal weld and an Alloy 52 Dissimilar Metal Weld with Buttering, in: International Symposium Contribution of Materials Investigations and Operating Experience to LWRs' Safety, Performance and Reliability, FONTEVRAUD 10, Avignon, France, 2022.
[32] P. Nevasmaa, P. Holmström, P. Karjalainen-Roikonen, T. Sarikka, M. Ahonen, R. Mouginot, U. Ehrnstén, A. Brederholm, P. Aaltonen, H. Hänninen, Fracture mechanical characterisation of ferrite-austenite dissimilar metal welds (DMWs) for elevated temperature service in view of metallurgical mismatch, in: International Conference on Life Management and Maintenance for Power Plants, Helsinki, 2013.
[33] K. Choi, J. Kim, B. Lee, C. Bahn, J. Kim, Effects of thermal aging on microstructures of low alloy steel–Ni base alloy dissimilar metal weld interfaces, J. Nucl. Mater. 441 (2013) 493–502.